

Confinement Fluorescence Effect: Polymer Crystalline Structure Visualization by an Aggregation-Induced Emission Luminogen

Lan Zhou¹, Linlin Zheng¹, Xiaoxiao Yu¹, Mengyue Gao¹, Chengjian Xu¹, Yifan Ge¹, Tianxiang Bai¹, Jin Wen¹, Yanhua Cheng¹, and Meifang Zhu¹

¹Donghua University - Songjiang Campus

January 20, 2023

Abstract

Direct visualization of polymer crystalline structure remains challenging due to the lack of contrast across different microphases of polymers. Here we address this conundrum using an aggregation-induced emission luminogen (AIEgen) with confinement fluorescence effect, which could be used as a “built-in” sensor to label different crystalline phases. Computational simulations reveal that the confined space induces the AIEgens to take a more planar conformation, resulting in a red-shifted emission spectrum. With this property, the information of various polymer crystalline forms is converted into different fluorescence colors, which is attributed to the different spatial dimensions of the polymer amorphous layer between lamellar crystals where the AIEgens are located. Finally, polymer crystalline phases distinction, quantitative crystallinity determination, and stereocomplex crystals visualization are achieved, providing a relationship between crystalline microstructure and fluorescence signals. This work demonstrates the potential of AIE fluorescence technology in polymer science, providing a theoretical and experimental guideline for the materials processing and optimization of mechanical performance.

Confinement Fluorescence Effect: Polymer Crystalline Structure Visualization by an Aggregation-Induced Emission Luminogen

Lan Zhou, Linlin Zheng, Xiaoxiao Yu, Mengyue Gao, Chengjian Xu, Yifan Ge, Tianxiang Bai, Jin Wen*, Yanhua Cheng*, Meifang Zhu

State Key Laboratory for Modification of Chemical Fibers and Polymer Materials, College of Materials Science and Engineering, Donghua University, Shanghai, 201620, China

Email: cyh@dhu.edu.cn; jinwen@dhu.edu.cn

Keywords: aggregation-induced emission, confinement fluorescence effect, polymer crystalline structure visualization

Abstract

Direct visualization of polymer crystalline structure remains challenging due to the lack of contrast across different microphases of polymers. Here we address this conundrum using an aggregation-induced emission luminogen (AIEgen) with confinement fluorescence effect, which could be used as a “built-in” sensor to label different crystalline phases. Computational simulations reveal that the confined space induces the AIEgens to take a more planar conformation, resulting in a red-shifted emission spectrum. With this property, the information of various polymer crystalline forms is converted into different fluorescence colors, which is attributed to the different spatial dimensions of the polymer amorphous layer between lamellar crystals where the AIEgens are located. Finally, polymer crystalline phases distinction, quantitative crystallinity determination, and stereocomplex crystals visualization are achieved, providing a relationship between crystalline microstructure and fluorescence signals. This work demonstrates the potential of AIE fluorescence technology in polymer science, providing a theoretical and experimental guideline for the materials processing and optimization of mechanical performance.

1. Introduction

Crystalline microstructure is an indispensable aspect of semicrystalline polymers, determining their mechanical properties and versatile functions.^[1-3] Tuning their properties is subject to crystalline engineering at the microscale length. Examples include solar cells performance improvement by manipulating semiconducting polymer crystal size and distribution;^[4] alcohol vapor sensing via conductive polymer crystallinity changes;^[5] mechanical toughness enhancement through crystalline structure transition.^[6] Thus, exploring the microstructure of semi-crystalline polymer materials is very important from the fundamental theory and engineering practice perspectives. However, direct crystalline structure visualization using general characterization methods is hindered, owing to the low specificity of the non-conductive polymer under electron beam,^[7] destructive process of targeted samples during thermal analysis, and complicated analysis and calculation procedures of X-ray related methods.

Fluorescence technology is a practical method that offers an accurate, simple, and easy-to-read approach for morphology visualization of the hydrated soft tissues.^[8-10] Such a technique could not only identify the external geometry of the targets, but also the associated internal microstructure.^[11,12] Generally, fluorescent dyes are used as “built-in” sensors to interact with the substances of the targets, extracting the interested information about their microenvironments.^[13-15] However, few examples have been demonstrated in the solid polymers, owing to the lacking in effective fluorophores for the condensed state polymers.^[16] Therefore, developing new fluorescent systems that are sensitive to the microenvironments of solid-state polymer is highly rewarding, which would facilitate the visualization of the polymer crystal structure.

Aggregation-induced emission luminogens (AIEgens) are well suited for this purpose due to the rotator and twisted molecular conformation,^[16] their working mechanism is the restriction of intramolecular motion (RIM).^[17] Upon excitation, non-radiative decay is depressed to facilitate fluorescence, as evidenced by the enhanced emission intensity of AIEgens in viscose

media or at low temperatures.^[18,19] Several AIE-based systems have been successfully demonstrated for condensed matter structure visualization,^[16] including micro-phase distribution imaging,^[20-22] inorganic-organic phase characterization,^[23] polymer viscosity change tracking,^[24] self-assembly evolution monitoring,^[25-27] and polymer gelation process observation.^[28] However, these systems typically utilize the processes that result from the changes in their chemical composition.

Luminescent materials are capable of exhibiting remarkable changes in fluorescent color and intensity under spatial confinement through the conformational change.^[29] Our previous studies showed that the polymorphic AIE system (TPE-EP) exhibits a pronounced color change when confined in the crystalline polymer phase, which originates from the changes of the molecular conformation and packing mode confined between the lamellar crystals. However, the mechanism of the color change due to confinement remains elusive. Herein, we use theoretical models with a hybrid scheme, in combination with quantum mechanics and molecular mechanics to explore the relationship between confined space, molecular packing, and frontier molecular orbitals of TPE-EP. Owing to high practical application value, biodegradable semi-crystalline polymers of poly(L-lactide) (PLLA) and poly(D-lactide) (PDLA) are selected to create confined spaces to accommodate TPE-EP for visualizing the polymer crystallinity, PLLA homocrystals (HCs) structure, and PLLA/PDLA stereocomplex crystals (SCs). It is noted that the formation of SCs forces molecular chains in the PLLA/PDLA blends to adopt a closed arrangement, forming a physical cross-linking network for significant improvement in mechanical properties. The proposed working mechanism is shown in Figure 1. This work provides a theoretical and experimental guideline for materials processing to optimize the mechanical properties of polymeric materials.

2. Results and Discussion

2.1. Electronic Structures based on QM/MM Simulations

In our previous work, it has been demonstrated that the green-emissive TPE-EP in the crossed-packing mode is favored in the amorphous phase of PLLA, while the yellow-emissive TPE-EP in the parallel-packing mode is preferred in the crystalline phase of PLLA.^[20,30] In the crystalline phase of PLLA, the molecules of TPE-EP are pushed in the amorphous areas between crystalline layers during polymer crystallization, the confined space forces TPE-EP molecules to adopt a more closed packing mode, resulting in red-shifted emission when compared with those molecules in amorphous PLLA. In order to understand the confinement fluorescence effect, we studied the molecular behavior in the complex system before and after space compression (Figure 2A). Specifically, the crystalline lattice parameters were reduced by 20% in three axes respectively with parameters in the original and compressed lattices listed in Table S1. We compared the torsion angles before and after the compression in different lattices (Table S2). The results show that the torsion angles defined in Figure 2A turn to be closer to 0° or 180°, increasing the conformational planarity of the four twisted moieties in TPE-EP.

According to the measurement of the distances between two neighboring TPE-EP molecules in the crystal lattice (Figure 2B and Figure S2), it is noted that the distance along the $\pi \cdots \pi$ stacking direction decreases more than the distance along the other directions, resulting in the change in the twisted conformation. As Figure 2B shows, the center distances between phenyl rings of TPE-EP are reduced from 7.09 and 6.71 Å to 5.75 and 5.92 Å respectively along the $\pi \cdots \pi$ stacking direction. The smaller intermolecular distance of TPE-EP, the closer the torsion angles between phenyl rings is to 0° or 180°. Therefore, we guess that the twisted conformation becomes more planar in the confined space to reduce compression-induced steric effects.

Intermolecular interactions have been used to demonstrate the effect on the optical properties of tetraphenylethene.^[31] Therefore, we further calculated the intermolecular interactions between the neighboring dimers in different packing conformations (Figure 2C and Figure S3) at the B3LYP/6-31G(d,p) level. It showed that the van der Waals interactions between TPE-EP

dimers could be decomposed into C-H $\cdots\pi$, C-H \cdots C, and $\pi\cdots\pi$ attractions. Similar to the theoretical investigation by Zheng and her coworkers,^[32] the van der Waals interactions dominate intermolecular interactions compared to electrostatic repulsion. As Figure 2C shows, the weak intermolecular interaction between the TPE-EP dimers in the native and compressed conformations along the *c*-axis is indicated by the interaction region indicator (IRI) using the electron density and gradient, which is defined in equation (1).^[33]

$$\text{IRI}(r) = \frac{|\nabla\rho(r)|}{[\rho(r)]^a} \quad (1)$$

where ρ is the electron density, r is the coordinate vector, a is an adjustable parameter, and the $\text{sign}(\lambda_2)$ is the sign of Hessian second largest eigenvalue of ρ , which are used to distinguish bonding ($\lambda_2 < 0$) and non-bonding ($\lambda_2 > 0$) interactions. The magnitude of $\text{sign}(\lambda_2)\rho$ is mapped on IRI isosurface with different colors for presenting the nature of the interaction region. The relatively stronger intermolecular interactions are demonstrated by relatively higher ρ and larger $\text{sign}(\lambda_2)\rho$ in Figure 2C. The results demonstrate that in our proposed polymorphic luminescent material, the weak intermolecular interactions are enhanced when the TPE-EP dimer is in a compressed confined space. We expect that when the twisted conformation is planarized during lattice compression, the emission spectrum should be red-shifted.

In addition to the conformational changes, analysis of the electronic structure, such as the energy of the highest occupied molecular orbital (HOMO) and lowest unoccupied molecular orbital (LUMO), will provide useful information for predicting confinement fluorescence effect. Frontier molecular orbitals, HOMO and LUMO reveal the charge transfer character in the excited state (Figure 2D and Figure S4). Before compression, the HOMO-LUMO gap of TPE-EP is 2.33 eV, while it decreases to 2.11 eV after compression along the *c*-axis, indicating that compression reduces the HOMO-LUMO energy gap. We infer that the overall effect on TPE-EP compression is the reduction in the energy gap, resulting in a red-shifted emission. Based on the computational simulations from the hybrid model, it demonstrates that the red-shifted

emission band is attributed to confined space-induced conformational planarization.

2.2. Crystallinity and crystal form visualization of PLLA homocrystals

From the above theoretical calculations, it has been demonstrated that the fluorescence emission is highly dependent on the confinement space size. Through manipulating the temperatures of isothermal crystallization, the size of the space between adjacent crystalline layers could be controlled accordingly. For example, the α and δ crystal forms of PLLA could be obtained by different crystallization temperatures. As shown in the layered stack model (Figure 3A), the long period (L), the amorphous layer thickness (L_a), and the crystal thickness (L_c) are identified. In PLLA α form, L_a between two crystalline layers is larger than that of δ form. It is anticipated that TPE-EP molecular packing could be manipulated if they are confined in such amorphous region, resulting in different fluorescence emissions accordingly.

With this special property, we incorporated TPE-EP into PLLA polymer matrix, followed by melt crystallization process between two glass slides. Crystallization temperature and isothermal crystallization time were controlled respectively, resulting in PLLA α or δ crystal form with different crystallinities. In our study, PLLA α crystal form was yielded by annealing the melt-quenched sample at a relatively high temperature of 130 °C. The crystalline regions with yellow emission are distinguished from green-emissive amorphous phases as radial spherulites grow (Figure 3B and Figure S5A). The spherulite crystalline morphology observed under the fluorescent microscope is in agreement with that under the polarized optical microscope. Figure 3C demonstrates the fluorescence sensitivity of TPE-EP in PLLA α crystal form by increasing the crystallization time. A gradually red-shifted emission from green to yellow was revealed. A similar red-shifted trend was observed when doping TPE-EP in PLLA δ crystal form, melt-quenched blends of TPE-EP and PLLA were annealed at a low temperature of 90 °C. With the increase of the crystallization time, numerous granular crystals in yellow emission were generated in green-emissive amorphous film (Figure 3D and Figure S5B), leading to red-shifting in fluorescence emission (Figure 3E). It is noted that the δ crystallite size

is smaller than that of the α crystal form, which is beneficial for the remarkably tough mechanical property of polylactide materials.^[34]

Crystallinity (χ_α) of these PLLA samples in α form was calculated by Wide-angle X-ray diffraction (WAXD) and differential scanning calorimetry (DSC). In Figure 3F, at the beginning of crystallization, the melt-quenched film is amorphous without diffraction peaks of the crystalline phase. With the crystallization process proceeding at around 130 °C, the crystalline peaks of the α form started to appear at 2θ values of 14.8°, 16.8°, 19.1°, and 22.4°, and the intensity increased with crystallization time. The DSC thermograms of a series of crystallized samples are in good agreement with the above WAXD results (Figure S6, Table S3 and equation S1). Their detailed fluorescence properties were tracked by photoluminescence (PL) spectroscopy. Figure 3G shows the normalized PL spectra of TPE-EP in PLLA α crystalline samples at a crystallinity of 4.60%, 12.7%, 22.9%, 37.0%, 46.2%, and 55.5%, respectively. With an increase of χ_α (α crystal form), a red-shifted light emission was observed from 523 nm to 542 nm in the PL spectrum. In addition, a linear correlation between PLLA crystallinity (α form) and wavelength maximum highlighted the quantitative sensing capability of TPE-EP (Figure 3H). The crystallinity (Figure S7, Table S4 and equation S2) and fluorescence emission maximum (Figure S8) of the as-prepared δ crystalline films were measured. A similar linear relationship was also observed for TPE-EP-doped PLLA δ crystal form. The 0.4 slope value of PLLA δ crystal form is larger than that of PLLA α crystal form (slope value = 0.3), which is ascribed to the smaller thickness of amorphous layer between two crystalline layers. More confined space pushed TPE-EP to adopt closer molecular packing with redder emission, which is supported by Small-angle X-ray Scattering (SAXS) measurement. After Lorentz-corrected analysis, L_a of α and δ crystal forms were calculated to be 13.8 nm and 12.7 nm (Figure 3I, Figure S9 and equation S3, χ_α , $\chi_\delta = 30\%$), respectively. The above results indicate the ability of TPE-EP to visualize the crystallinity of PLLA HCs with different crystal forms based on the confinement fluorescence effect.

2.3. Fluorescence visualization of PLLA/PDLA stereocomplex crystallites

To improve the thermal stability, thermal resistance, and mechanical strength of polylactide materials, the formation of SCs between enantiomeric PLLA and PDLA is one of the most effective and promising strategies.^[34-38] It is noted that SCs are created from the PLLA/PDLA blends. The SCs provide the higher melting point (~ 230 °C) than that of the α or δ form consisting of PLLA homopolymer (~ 170 °C). Besides, SCs also exhibit superior mechanical properties compared to HCs. The improved physical properties of SCs form are mainly attributed to the compact molecular packing and strong interchain interactions between the left-handed PLLA and right-handed PDLA polymer chains (Figure 4A).^[39] Therefore, the crystalline structure of SC is important for understanding the crystal structure-physical property relationships of polylactide materials.

In order to evaluate the sensing ability of TPE-EP in SCs, the blend samples of PLLA/PDLA with the various L/D ratios were fabricated from casting the solutions. Here, the L/D ratio stands for the mixing ratio between PLLA and PDLA (weight percent). Figure 4B shows the fluorescence response of TPE-EP in a range of L/D blends. The blend samples with the L/D ratio of 100/0–60/40 showed a blue-shifted emission with increasing D content, while the opposite trend was observed for the blends with L/D ratio of 40/60–0/100. Yet, the L/D 50/50 gave the reddest emission of 559 nm. Afterwards, the WAXD analyzes were carried out for these blend samples to correlate the information between crystalline structure and fluorescence behavior (Figure 4C and Figure S10). The results show that homopolymer of PLLA or PDLA gave the pure α phase, while the L/D 60/40–40/60 blend samples exhibited only the SC phase. Meanwhile, the samples with the L/D ratio 90/10-70/30 and 30/70-10/90 showed the mixture of the α and SC crystallites. Figure 4D summarizes the results of the WAXD characterizations. The integrated area of the (200/110), (203), and (210) diffraction peaks of the α form ($A(\alpha)$), and those of the (110), (300/030), and (220) diffraction peaks of the SC phase ($A(\text{SC})$), and

those of amorphous part $A(\text{am})$ were evaluated from the WAXD profiles shown in Figure 4C. The ratio $A(\text{SC})/[A(\text{SC}) + A(\alpha) + A(\text{am})]$, that is, the crystallinity of SCs phase (χ_{SC}), was plotted versus the L/D ratio in the blend sample. The crystallinity of the α form, $\chi_{\alpha} (= A(\alpha)/[A(\text{SC}) + A(\alpha) + A(\text{am})])$, as well as the sum of the SC fraction (χ_{SC}) and α fraction (χ_{α}) are also plotted here with blue hollow triangles and red squares, respectively. The crystalline structure of the samples of L/D 100/0–60/40 is symmetric to the cases of L/D 40/60-0/100. That is, the SC formation area is symmetrical about the center of L/D 50/50. The DSC analyses shown in supporting information (Figure S11 and Table S5-S7) are consistent with the WAXD data (Figure 4C). It is noted that the correlation between the emission maximum and the D component is consistent with that of crystalline structure (Figure 4E and Table S8), confirming the capability of TPE-EP in sensing stereocomplex of PLLA/PDLA.

As illustrated in Figure 4A, TPE-EP molecules are repelled to the amorphous layer in the layered stack model. After Lorentz-corrected analysis of SAXS data of L/D blend samples, we found that the changes in amorphous lamellar thickness account for the fluorescence process of TPE-EP (Figure 4E, Figure S12 and Table S9). TPE-EP in L/D 50/50 shows the red-shifted emission with the maximum wavelength ($\lambda_{\text{em}} = 559 \text{ nm}$) because L/D 50/50 has the smallest L_{a} (15.8 nm), which is consistent with the fluorescence phenomenon. It is worth mentioning that TPE-EP molecules in pure SC phase gave redder emission than those in α crystal form or δ crystal form, even though the larger amorphous layer thickness was displayed in SC phase. The reason might be attributed to the tight molecular packing and strong molecular interaction among the L/D stereocomplex. The rigid microenvironment of L/D amorphous layer also promotes the red-shifted emission of TPE-EP,^[20] which was supported by their apparent mechanical properties. The rigidity of L/D blend polymers was compared by nanoindentation test. In a typical measurement, The load applied to the tip of the indenter increases as the tip penetrates further into the sample and soon reaches a pre-defined value. After the tip was retracted, the area of the residual indentation was measured. Figure 4F shows load-displacement

curves for instrumented nanoindentation tests of the blends with the L/D ratio 50/50, 60/40, and 70/30. The specimen hardness (H) can be defined by the following equation (2).^[40]

$$H = \frac{P_{\max}}{A_c} \quad (2)$$

where P_{\max} is the load maximum and A_c is the residual indentation area. The results indicate stereocomplex of L/D 50/50 has the greatest mechanical performance, supporting the fluorescence behavior shown in Figure 4E. The synergistic effect of confined space and rigid microenvironment facilitate TPE-EP to visualize the stereocomplex crystalline polylactide materials.

3. Conclusion

In conclusion, we have shown how TPE-EP is a unique sensor to visualize polymer crystalline structure. A hybrid model combined with quantum mechanics and molecular mechanics reveals that the confined space increases the planarity of the twisted AIEgen, resulting in a red shift in the emission spectrum. During polymer crystallization, the amorphous layer confined between two crystalline lamellae provides a free space to accommodate TPE-EP molecules. The information on the polymer crystalline structure is marked in different colors, originating from the conformational changes of TPE-EP within the confined amorphous layer of various crystalline forms. As a result, visualization of crystallinity, differentiation of PLLA α and δ forms, and visualization of stereocomplex crystals are achieved by fluorescence color changes. We envisage that this concept will be applicable to *in-situ* monitoring of the polylactide material manufacturing process, as well as predicting the macroscopic polymer physical properties. Ultimately, it helps to optimize processing parameters and improve production efficiency.

Experimental Section

Computational Details: The packing conformation of TPE-EP was simulated using the model shown in Figure S1, according to the previously reported polymorphic arrangements of TPE-EP.^[30] To save the computational process, a hybrid quantum mechanics/molecular mechanics

(QM/MM) approach with an ONIOM scheme was applied,^[41] in which the center TPE-EP and PF₆⁻ anion were calculated at the B3LYP/6-31G(d,p) level and the other molecules were simulated by a universal force field (UFF). We reduced the crystal lattice by 15-20% along the three lattice axes of TPE-EP, denoted as *a*-, *b*-, and *c*-directions in Figure S1 for simulating compression in experiments. We then optimized the QM regions within the QM/MM (B3LYP/UFF) scheme, while the MM regions were frozen in comparison with the original lattice. Following the optimization, vibrational modes were checked to confirm that the optimized structure was minimum. The change in the energy gap between frontier molecule orbitals could be used as an indicator in molecular spectroscopy, followed by a comparison in the energy difference between the highest occupied molecular orbital (HOMO) and the lowest unoccupied molecular orbital (LUMO) at the B3PW91/cc-pVTZ level. Since the B3PW91/cc-pVTZ method has provided reasonable HOMO-LUMO gaps in conjugated oligomers in a previous study,^[42,43] we also applied this approach in calculations for a single TPE-EP molecule, which was extracted from the optimized QM/MM model. All calculations were carried out using the program Gaussian 16 in version C.02.^[44] Our simulations could provide the insight of the confinement effect on fluorescence spectroscopy, which could be used as a rational design in visualization and performance control of the polymer processing.

Preparation of α and δ crystal forms of TPE-EP-doped PLLA: The TPE-EP powder was dissolved in tetrahydrofuran (THF) to produce a stock solution (1 mg mL⁻¹). Meanwhile, PLLA ($M_w = 1.1 \times 10^5$ g mol⁻¹, PDI = 2.92) was dissolved in trichloromethane to make a polymer solution (10 mg mL⁻¹). Afterwards, a specified amount of TPE-EP solution and PLLA solution was mixed at room temperature, in which the TPE-EP content was 0.5 wt%. The mixture was cast on a quartz sheet to form a film sample by slow evaporation. The obtained film samples were then melted between glass slides at 185 °C for 2 min, and rapidly cooled to 130 °C for isothermal crystallization. By controlling different crystallization times, a series of PLLA α crystalline samples with different crystallinities were obtained. To control the formation of

PLLA δ crystals, the isothermal crystallization temperature was controlled at 90 °C. The crystallization time was adjusted to obtain PLLA δ crystalline samples with different degrees of crystallinity.

Preparation of TPE-EP-doped poly(lactic acid) stereocomplex crystals: PLLA ($M_w = 2.9 \times 10^3$ g mol⁻¹, PDI = 5.92) and PDLA ($M_w = 4.5 \times 10^4$ g mol⁻¹, PDI = 1.60) were respectively dissolved in trichloromethane to form 10 mg mL⁻¹ polymer solutions. They were then mixed in the desired ratios to form a range of PLLA/PDLA blends. Afterwards, a certain amount of TPE-EP stock solution was added to the above solutions under vigorous stirring, wherein the TPE-EP content was controlled at 0.5 wt%. Finally, 1.5 mL of the mixed solution was placed in a 2 mL vial, and the solvent was evaporated at 60 °C for crystallization.

Measurements: WAXD was measured on a Bruker D2 phaser X-ray diffractometer using Cu K α radiation. DSC was carried out on a DSC Q20 (TA Instruments) at a heating rate of 10 °C min⁻¹ under nitrogen atmosphere. SAXS characterizations were performed on a SAXSessmc2 instrument (Anton Paar). Fluorescence photographs were captured by a Canon EOS 80D camera. PL spectra was recorded using a PTI QM/TM. Fluorescence and polarizing microscope images were taken on a Nikon Eclipse Ni-U microscope. Nanoindentation measurements were performed on a Bruker Hysitron TI980 instrument.

Acknowledgements

This work was partially supported by the National Science Foundation of China (51973030, 52127805, 52273031, 22173017), the Science and Technology Commission of Shanghai Municipality (20JC1414900, 22511103900), the Shanghai Rising-Star Program (20QA1400100), the China Postdoctoral Science Foundation (2022M710664, 2022M710663, 2022T150111), the Fundamental Research Funds for the Central Universities (2232021A-06, 22D210613), “DHU” Distinguished Young Professor Program (LZB2021001) and State Key Laboratory for Modification of Chemical Fibers and Polymer Materials, Donghua University.

Conflict of Interests

The authors declare no conflict of interests.

Data Availability Statement

The data that support the findings of this study are available from the corresponding author upon reasonable request.

Supporting Information

Supporting Information is available from the Wiley Online Library or from the author.

Received: ((will be filled in by the editorial staff))

Revised: ((will be filled in by the editorial staff))

Published online: ((will be filled in by the editorial staff))

References

1. C. L. F. De Ten Hove, J. Penelle, D. A. Ivanov, A. M. Jonas, *Nat. Mater.* **2004**, 3, 33.
2. K. P. Cui, Z. Ma, N. Tian, F. M. Su, D. Liu, L. B. Li, *Chem. Rev.* **2018**, 118, 1840.
3. Y. F. Xu, D. Kraemer, B. Song, Z. Jiang, J. W. Zhou, J. Loomis, J. J. Wang, M. D. Li, H. Ghasemi, X. P. Huang, X. B. Li, G. Chen, *Nat. Commun.* **2019**, 10, 1771.
4. Y. H. Liu, J. B. Zhao, Z. K. Li, C. Mu, W. Ma, H. W. Hu, K. Jiang, H. R. Lin, H. Ade, H. Yan, *Nat. Commun.* **2014**, 5, 5293.
5. A. A. Athawale, M. V. Kulkarni, *Sens. Actuators B Chem.* **2000**, 67, 173.
6. S. Kimata, T. Sakurai, Y. Nozue, T. Kasahara, N. Yamaguchi, T. Karino, M. Shibayama, J. A. Kornfield, *Science* **2007**, 316, 1014.
7. O. Panova, X. C. Chen, K. C. Bustillo, C. Ophus, M. P. Bhatt, N. Balsara, A. M. Minor, *Micron* **2016**, 88, 30.
8. K. M. Dean, A. E. Palmer, *Nat. Chem. Biol.* **2014**, 10, 512.

9. Z. J. Qiu, W. J. Zhao, M. K. Cao, Y. Q. Wang, J. W. Y. Lam, Z. Zhang, X. Chen, B. Z. Tang, *Adv. Mater.* **2018**, 30, 1803924.
10. S. G. Yang, Z. Z. Wei, L. Cseh, P. Kazemi, X. B. Zeng, H. J. Xie, H. Saba, G. Ungar, *Nat. Commun.* **2021**, 12, 5054.
11. R. Ameloot, F. Vermoortele, J. Hofkens, F. C. De Schryver, D. E. De Vos, M. B. J. Roeffaers, *Angew. Chem. Int. Ed.* **2013**, 52, 401.
12. J. F. Dekkers, M. Alieva, L. M. Wellens, H. C. R. Ariese, P. R. Jamieson, A. M. Vonk, G. D. Amatngalim, H. L. Hu, K. C. Oost, H. J. G. Snippert, J. M. Beekman, E. J. Wehrens, J. E. Visvader, H. Clevers, A. C. Rios, *Nat. Protoc.* **2019**, 14, 1756.
13. J. S. Ni, P. F. Zhang, T. Jiang, Y. C. Chen, H. F. Su, D. Wang, Z. Q. Yu, R. T. K. Kwok, Z. J. Zhao, J. W. Y. Lam, B. Z. Tang, *Adv. Mater.* **2018**, 30, 1805220.
14. P. Kanchanawong, G. Shtengel, A. M. Pasapera, E. B. Ramko, M. W. Davidson, H. F. Hess, C. M. Waterman, *Nature* **2010**, 468, 580.
15. J. Qi, C. W. Sun, A. Zebibula, H. Q. Zhang, R. T. K. Kwok, X. Y. Zhao, W. Xi, J. W. Y. Lam, J. Qian, B. Z. Tang, *Adv. Mater.* **2018**, 30, 1706856.
16. J. Mei, N. L. C. Leung, R. T. K. Kwok, J. W. Y. Lam, B. Z. Tang, *Chem. Rev.* **2015**, 115, 11718.
17. Z. K. He, C. Q. Ke, B. Z. Tang, *ACS Omega* **2018**, 3, 3267.
18. Y. C. Chen, J. W. Y. Lam, R. T. K. Kwok, B. Liu, B. Z. Tang, *Mater. Horiz.* **2019**, 6, 428.
19. J. Q. Dong, X. Li, K. Zhang, Y. Di Yuan, Y. X. Wang, L. Z. Zhai, G. L. Liu, D. Q. Yuan, J. W. Jiang, D. Zhao, *J. Am. Chem. Soc.* **2018**, 140, 4035.
20. Y. H. Cheng, S. J. Liu, F. Y. Song, M. Khorloo, H. K. Zhang, R. T. K. Kwok, J. W. Y. Lam, Z. K. He, B. Z. Tang, *Mater. Horiz.* **2019**, 6, 405.
21. G. Iasilli, A. Battisti, F. Tantussi, F. Fuso, M. Allegrini, G. Ruggeri, A. Pucci, *Macromol. Chem. Phys.* **2014**, 215, 499.

22. T. Han, C. Gui, J. W. Y. Lam, M. J. Jiang, N. Xie, R. T. K. Kwok, B. Z. Tang, *Macromolecules* **2017**, 50, 5807.
23. W. J. Guan, S. Wang, C. Lu, B. Z. Tang, *Nat. Commun.* **2016**, 7, 11811.
24. S. J. Liu, Y. H. Cheng, H. K. Zhang, Z. J. Qiu, R. T. K. Kwok, J. W. Y. Lam, B. Z. Tang, *Angew. Chem. Int. Ed.* **2018**, 57, 6274.
25. D. P. Zhang, Y. J. Fan, H. Chen, S. Trépout, M. H. Li, *Angew. Chem., Int. Ed.* **2019**, 58, 10260.
26. H. Q. Peng, B. Liu, P. F. Wei, P. F. Zhang, H. K. Zhang, J. F. Zhang, K. Li, Y. Li, Y. H. Cheng, J. W. Y. Lam, W. J. Zhang, C. S. Lee, B. Z. Tang, *ACS Nano* **2019**, 13, 839.
27. Y. Jiang, N. Hadjichristidis, *Macromolecules* **2019**, 52, 1955.
28. Z. K. Wang, J. Y. Nie, W. Qin, Q. L. Hu, B. Z. Tang, *Nat. Commun.* **2016**, 7, 12033.
29. B. Fang, P. P. Li, J. M. Jiang, W. Du, L. M. Wang, H. Bai, B. Peng, X. Huang, Z. F. An, L. Li, X. K. Yang, L. Fu, W. Huang, *Coord. Chem. Rev.* **2021**, 440, 213979.
30. M. Khorloo, Y. H. Cheng, H. K. Zhang, M. Chen, H. H. Y. Sung, I. D. Williams, J. W. Y. Lam, B. Z. Tang, *Chem. Sci.* **2019**, 11, 997.
31. H. S. Yuan, K. Wang, K. Yang, B. B. Liu, B. Zou, *J. Phys. Chem. Lett.* **2014**, 5, 2968.
32. Y. Zeng, Y. L. Niu, Q. Peng, X. Y. Zheng, *J. Phys. Chem. A* **2022**, 126, 4147.
33. T. Lu, Q. X. Chen, *Chem.: Methods* **2021**, 1, 231.
34. K. Tashiro, N. Kouno, H. Wang, H. Tsuji, *Macromolecules* **2017**, 50, 8048.
35. J. Q. Liu, X. L. Qi, Q. J. Feng, Q. F. Lan, *Macromolecules* **2020**, 53, 3493.
36. R. Y. Bao, W. Yang, W. R. Jiang, Z. Y. Liu, B. H. Xie, M. B. Yang, *J. Phys. Chem. B* **2013**, 117, 3667.
37. X. F. Wei, R. Y. Bao, Z. Q. Cao, W. Yang, B. H. Xie, M. B. Yang, *Macromolecules* **2014**, 47, 1439.

38. Y. Z. Li, Q. Li, G. S. Yang, Ruihao. Ming, M. M. Yu, H. H. Zhang, H. L. Shao, *Adv. Polym. Technol.* **2018**, 37, 1674.
39. P. J. Pan, J. J. Yang, G. R. Shan, Y. Z. Bao, Z. X. Weng, A. Cao, K. Yazawa, Y. Inoue, *Macromolecules* **2011**, 45, 189.
40. J. F. Wang, C. Yang, Y. K. Liu, Y. Li, Y. Q. Xiong, *ACS Omega* **2022**, 7, 14317.
41. S. Dapprich, I. Komáromi, K. S. Byun, K. Morokuma, M. J. Frisch, *J. Mol. Struct.: THEOCHEM* **1999**, 461-462, 1.
42. J. M. Crowley, J. Tahir Kheli, W. A. Goddard, *J. Phys. Chem. Lett.* **2016**, 7, 1198.
43. S. Manzetti, T. Lu, *RSC Adv.* **2013**, 3, 25881.
44. Gaussian 16, Revision C.02, M. J. Frisch, G. W. Trucks, H. B. Schlegel, G. E. Scuseria, M. A. Robb, J. R. Cheeseman, G. Scalmani, V. Barone, G. A. Petersson, H. Nakatsuji, X. Li, M. Caricato, A. V. Marenich, J. Bloino, B. G. Janesko, R. Gomperts, B. Mennucci, H. P. Hratchian, J. V. Ortiz, A. F. Izmaylov, J. L. Sonnenberg, D. Williams-Young, F. Ding, F. Lipparini, F. Egidi, J. Goings, B. Peng, A. Petrone, T. Henderson, D. Ranasinghe, V. G. Zakrzewski, J. Gao, N. Rega, G. Zheng, W. Liang, M. Hada, M. Ehara, K. Toyota, R. Fukuda, J. Hasegawa, M. Ishida, T. Nakajima, Y. Honda, O. Kitao, H. Nakai, T. Vreven, K. Throssell, J. A. Montgomery, Jr., J. E. Peralta, F. Ogliaro, M. J. Bearpark, J. J. Heyd, E. N. Brothers, K. N. Kudin, V. N. Staroverov, T. A. Keith, R. Kobayashi, J. Normand, K. Raghavachari, A. P. Rendell, J. C. Burant, S. S. Iyengar, J. Tomasi, M. Cossi, J. M. Millam, M. Klene, C. Adamo, R. Cammi, J. W. Ochterski, R. L. Martin, K. Morokuma, O. Farkas, J. B. Foresman, and D. J. Fox, *Gaussian, Inc., Wallingford CT*, **2016**.

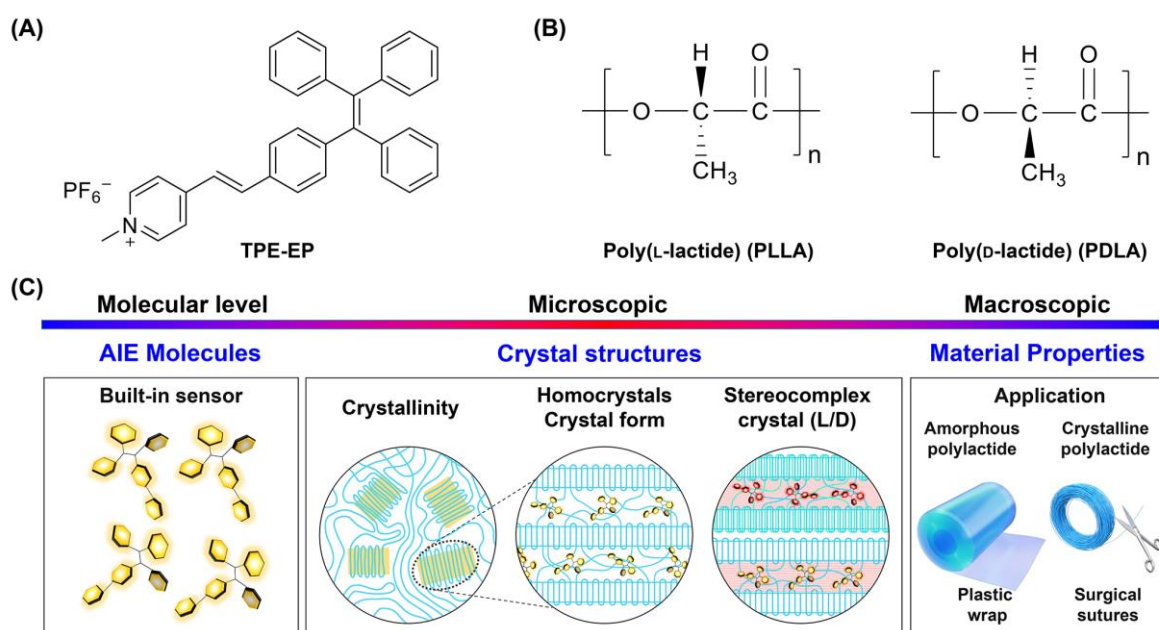


Figure 1. Confinement fluorescence effect-induced polylactide crystal structure visualization for polymer engineering and diverse applications. (A) Molecular structure of TPE-EP. (B) Chemical structure of PLLA and PDLA. (C) TPE-EP as a “built-in” sensor to visualize PLLA α and δ forms, crystallinity of PLLA homocrystals, and stereocomplex crystallites.

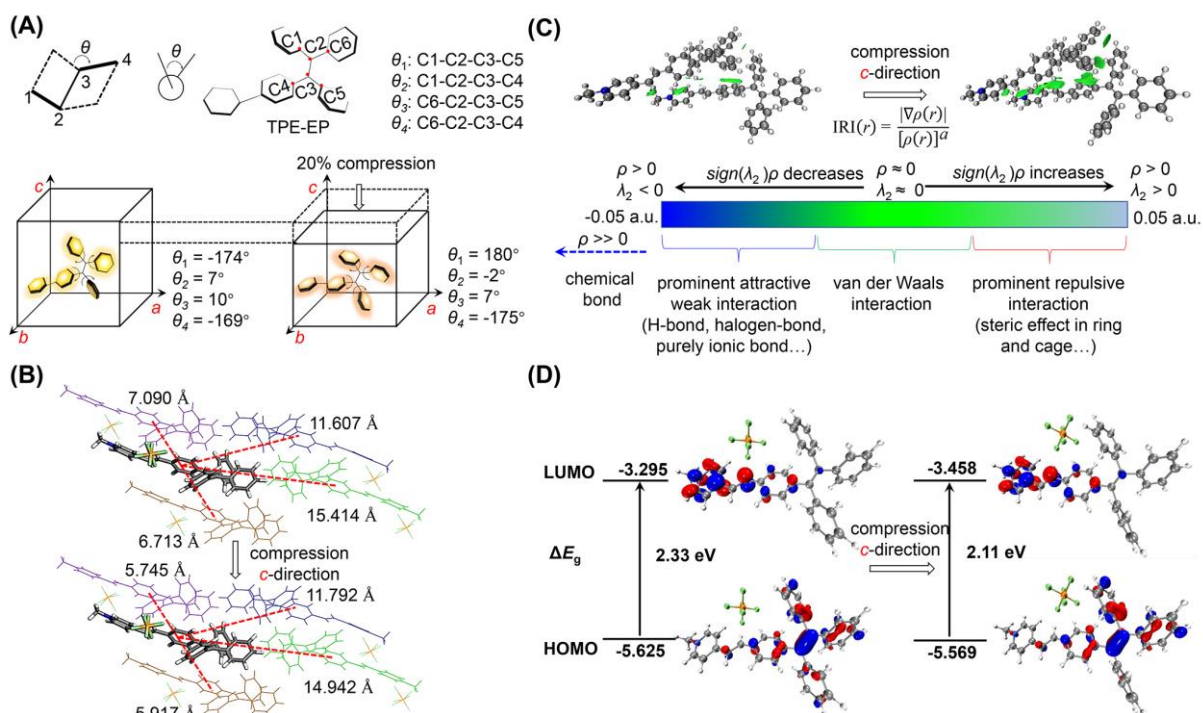


Figure 2. Confinement fluorescence effect. (A) Schematic diagram of the torsion definition (top) and the torsion angles of TPE-EP before and after compression along the c -direction (bottom). (B) Distances between neighboring TEP-EP dimers in the original (top) and compressed along c -direction (bottom) from molecular simulations in the QM/MM scheme. (C) IGMH analysis calculated at the B3LYP/6-31g(d,p) level with dispersion corrected between TPE-EP dimers in the original (left) and compressed along c -direction (right). The bottom is coloring and chemical interpretation of $\text{sign}(\lambda_2)\rho$ on the IRI isosurfaces. (D) Molecular orbitals of TPE-EP calculated at the B3PW91/cc-pVTZ level in the original (left) and compressed along c -direction (right).

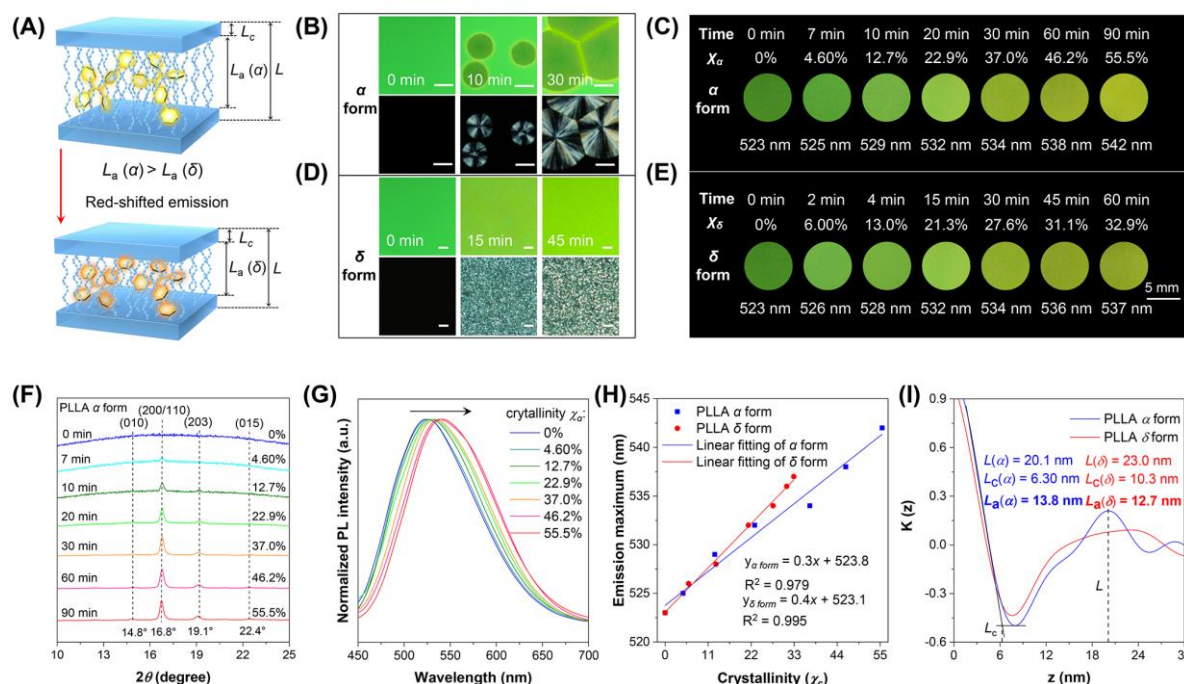


Figure 3. PLLA homocrystals visualization. (A) Layered stacking model of PLLA α and δ crystal forms with ideal phase boundary. TPE-EP molecules as built-in sensor are expelled into the amorphous layers for PLLA crystal form sensing. (B, D) Fluorescence (top) and polarized optical (bottom) micrographs of the neat PLLA during isothermal crystallization at 130 °C (B) and 90 °C (D), respectively. The scale bar is 50 μm . (C, E) Fluorescence images of TPE-EP-doped PLLA during isothermal crystallization at 130 °C (C) and 90 °C (E), respectively. UV excitation wavelength: 365 nm. (F) WAXD profile measured for PLLA α form with increasing crystallization time at a given crystallization temperature of 130 °C. (G) Normalized PL spectra of TPE-EP-doped PLLA (α crystal form) at different crystallinities. $\lambda_{\text{em}} = 400 \text{ nm}$. (H) Plots of the estimated crystallinity versus the emission maximum with linear fit relationships. (I) One-dimensional correlation function curves of PLLA α and δ crystal forms, which are calculated from their Lorentz-corrected SAXS curves.

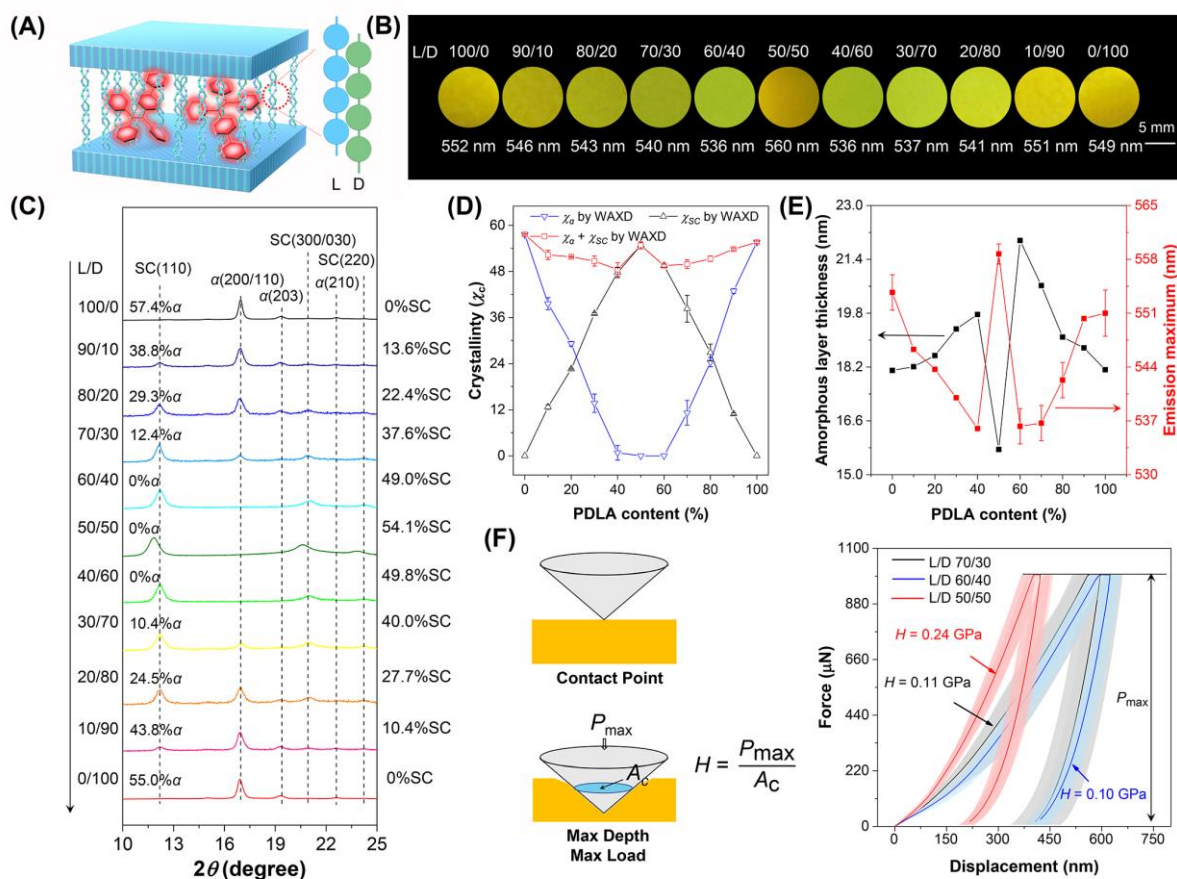


Figure 4. PLLA/PDLA stereocomplex crystallites visualization. (A) Layered stacking model of PLLA/PDLA SCs form with ideal phase boundary. TPE-EP molecules are constrained in amorphous layer between two crystalline lamellae. (B) Fluorescence images of a series of TPE-EP-doped PLLA/PDLA blends with different L/D ratios. Excitation wavelength: 365 nm. (C) WAXD profile measured for PLLA/PDLA blends with different L/D ratios. (D) Change of χ_α , χ_{SC} , $\chi_\alpha + \chi_{SC}$ of PLLA/PDLA blends with various L/D ratios. (E) Amorphous layer thickness and emission maximum versus the various L/D contents. (F) Schematic illustration of the nanoindentation test (left). The indentation force-displacement curves of PLLA/PDLA blends during nanoindentation test (right).

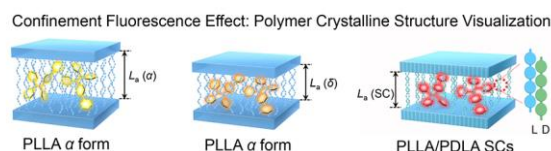
Polymer crystalline structure visualization is realized by using an AIE-active molecule as a “built-in” sensor through the conformational change without a change in molecule structure. This confinement-dependent emission of AIE molecules enables color-coding various crystalline forms of polymers, providing guidance for materials processing and mechanical property optimization.

Keywords: aggregation-induced emission, confinement fluorescence effect, polymer crystalline structure visualization

Lan Zhou, Linlin Zheng, Xiaoxiao Yu, Mengyue Gao, Chengjian Xu, Yifan Ge, Tianxiang Bai, Jin Wen*, Yanhua Cheng*, Meifang Zhu

Confinement Fluorescence Effect: Polymer Crystalline Structure Visualization by an Aggregation-Induced Emission Luminogen

TOC figure



Supporting Information

Confinement Fluorescence Effect: Polymer Crystalline Structure Visualization by an Aggregation-Induced Emission Luminogen

Lan Zhou, Linlin Zheng, Xiaoxiao Yu, Mengyue Gao, Chengjian Xu, Yifan Ge, Tianxiang Bai, Jin Wen*, Yanhua Cheng*, Meifang Zhu

State Key Laboratory for Modification of Chemical Fibers and Polymer Materials, College of Materials Science and Engineering, Donghua University, Shanghai, 201620, China.

Email: cyh@dhu.edu.cn; jinwen@dhu.edu.cn

1. Crystallinity measurements

The crystallinity (χ_c) of PLA samples was determined by DSC and WAXD. The degree of crystallinity was calculated using MDI Jade 6.0 software on the basis of the WAXD results. Meanwhile, the DSC analyses were simultaneously performed to confirm the WAXD data. Specifically, the crystallinity of PLLA α crystal form, δ crystal samples form, and SCs phase were calculated according to equation (1), (2), and (3), respectively.

$$\chi_{\alpha}(\%) = \frac{\Delta H_m - \Delta H_c}{\Delta H_m^0} \times 100\% \quad (1)$$

$$\chi_{\delta}(\%) = \frac{\Delta H_m - \Delta H_c - \Delta H_{m,\delta \rightarrow \alpha}}{\Delta H_m^0} \times 100\% \quad (2)$$

$$\chi_{SC}(\%) = \frac{\Delta H_{m,SC}}{\Delta H_{m,SC}^0} \times 100\% \quad (3)$$

ΔH_m is the melting enthalpy of PLLA, ΔH_c is the exothermic enthalpy deriving from crystallization of PLLA. $\Delta H_{m,\delta \rightarrow \alpha}$ is the exothermic enthalpy arising from the transition from δ crystal form to α crystal form. ΔH_m^0 corresponds to a melting enthalpy of 106 J g⁻¹ for 100% χ_c PLLA.^[1] $\Delta H_{m,SC}$ is the melting enthalpy of SC, and $\Delta H_{m,SC}^0$ corresponds to a melting enthalpy of 142 J g⁻¹ for 100% SCs polylactides.^[2,3]

2. Amorphous layer thickness calculation

To obtain the amorphous layer thickness (L_a), one-dimensional correlation function was extracted from the experimental SAXS patterns by equation (4).^[4]

$$\gamma(z) = \frac{\int_0^\infty I(q)q^2 \cos(qz) dq}{\int_0^\infty I(q)q^2 dq} \quad (4)$$

where $I(q)$ is the scattering intensity, z is the direction that perpendicular to the laminar interface.

The detailed calculation process was referred to our previously reported work.^[5]

3. Supplementary Figures and Tables

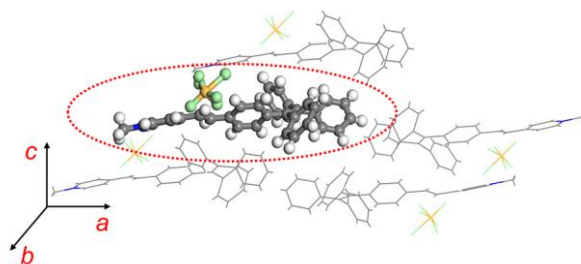


Figure S1. Simulation models of TPE-EP. The simulated TPE-EP is represented as ball- and stick-models in the QM region, while the molecules surrounded by the research object are represented as line models in the MM region.

Table S1. Lattice parameters (in Å) in TPE-EP models in the original- and compressed-conformation along a -, b -, and c -directions, denoted as P(a)-P(c), respectively.

	a	b	c
original	24.89	9.18	12.58
P (a)	20.89	9.18	12.58
P (b)	24.89	7.60	12.58
P (c)	24.89	9.18	10.40

Table S2. Torsion angles (in degrees) of TEP-EP obtained by QM/MM optimization in original- and compressed-conformation along *a*-, *b*-, and *c*-directions, denoted as P(*a*)-P(*c*), respectively.

	θ_1	θ_2	θ_3	θ_4
original	-174	7	10	-169
P (<i>a</i>)	175	-3	-4	177
P (<i>b</i>)	-174	7	8	-171
P (<i>c</i>)	180	-2	7	-175

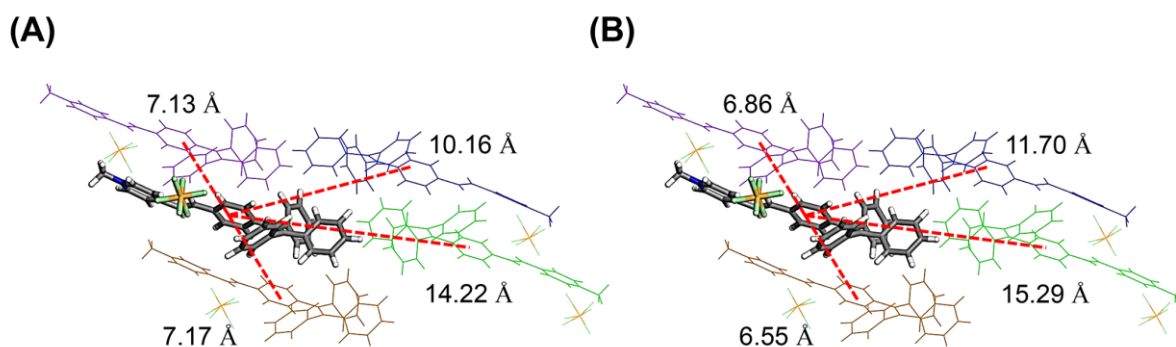


Figure S2. Distances between neighboring TEP-EP dimers compressed along (A) *a*-direction and (B) *b*-direction from molecular simulations in the QM/MM scheme.

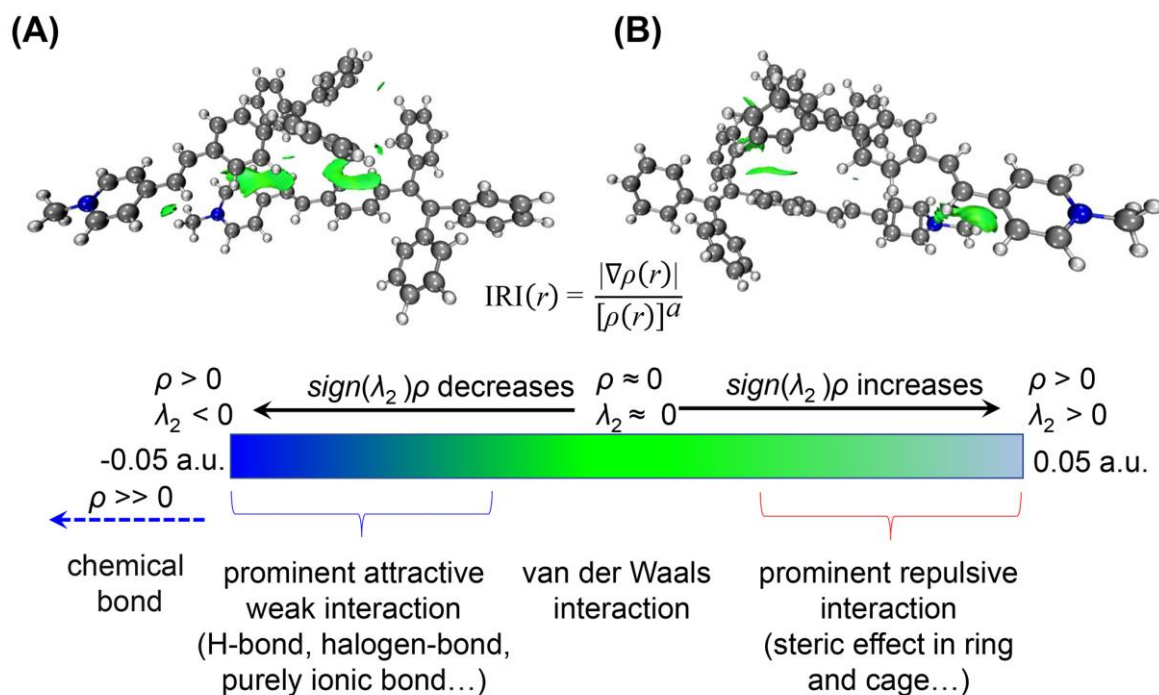


Figure S3. IGMH analysis calculated at the B3LYP/6-31g(d,p) level with dispersion corrected between TPE-EP dimers compressed along (A) *a*-direction and (B) *b*-direction. The bottom is coloring and chemical interpretation of $sign(\lambda_2)\rho$ on the IRI isosurfaces.

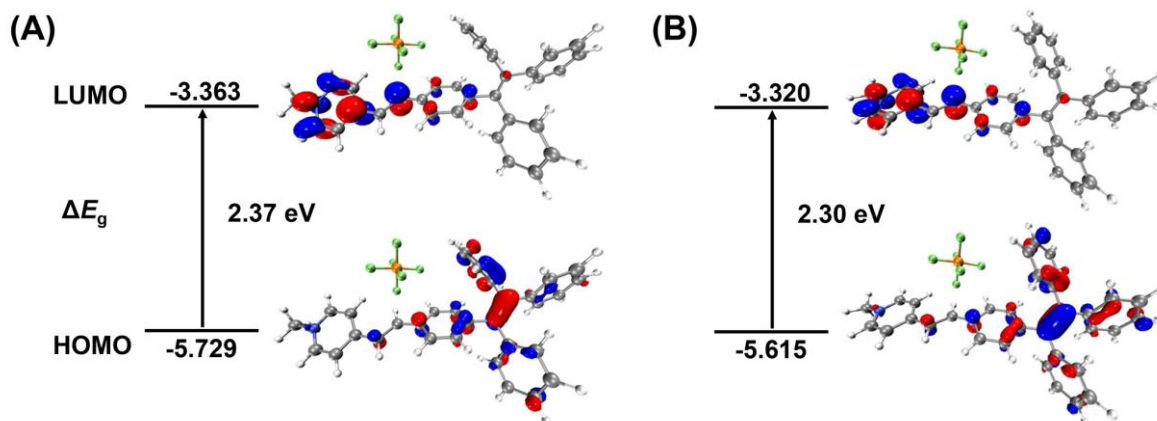


Figure S4. Molecular orbitals of TPE-EP calculated at the B3PW91/cc-pVTZ level compressed along (A) *a*-direction and (B) *b*-direction respectively.

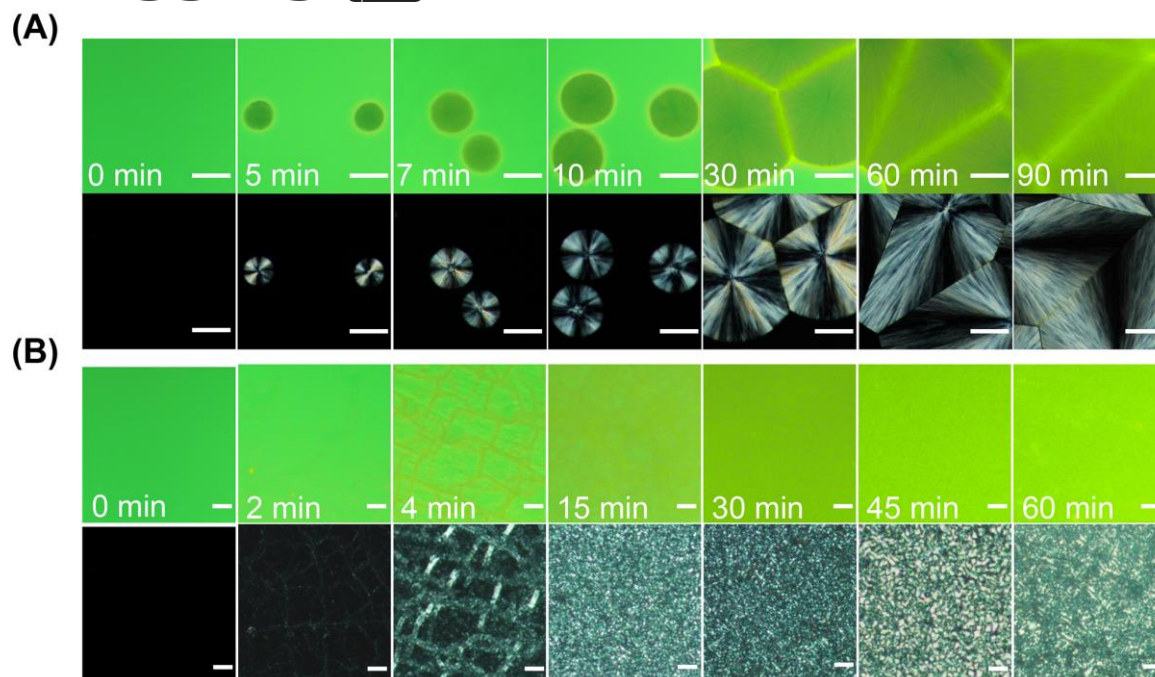


Figure S5. Fluorescence (top) and polarized light micrographs (bottom) of TPE-EP-doped PLLA during isothermal crystallization at 130 °C (A) and 90 °C (B), respectively.

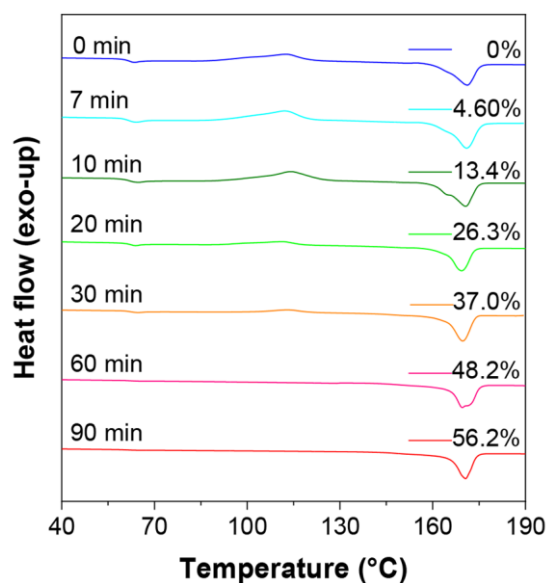


Figure S6. DSC thermograms of PLLA α crystal form with increasing crystallization time, which were recorded during the first heating scan.

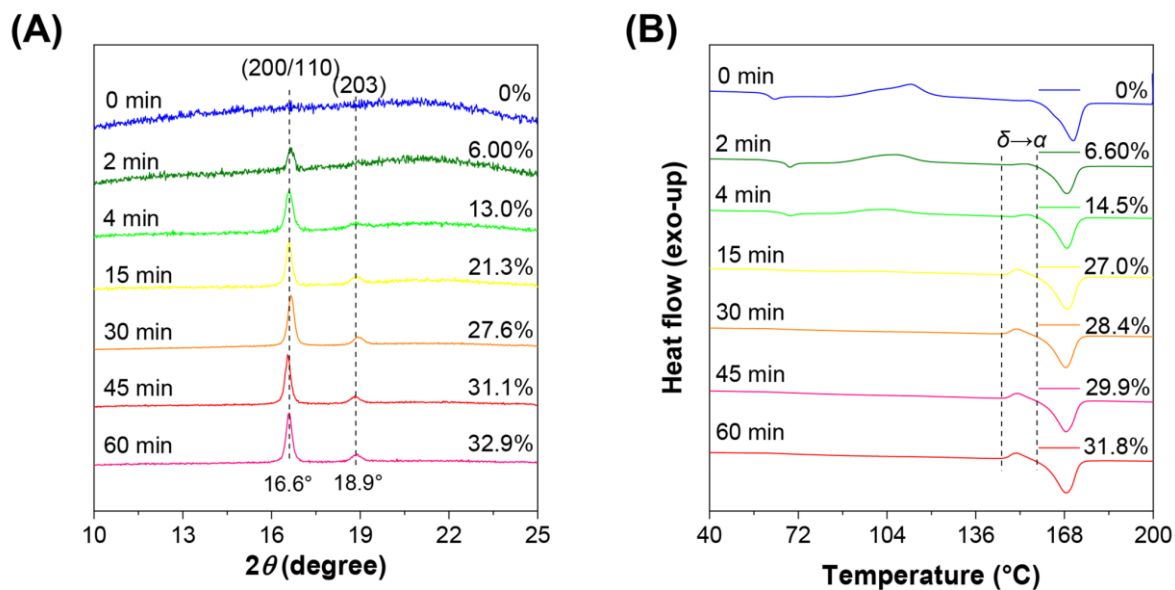


Figure S7. (A) WAXD patterns and (B) DSC thermograms (first heating scan) measured for PLLA δ form with increasing crystallization time.

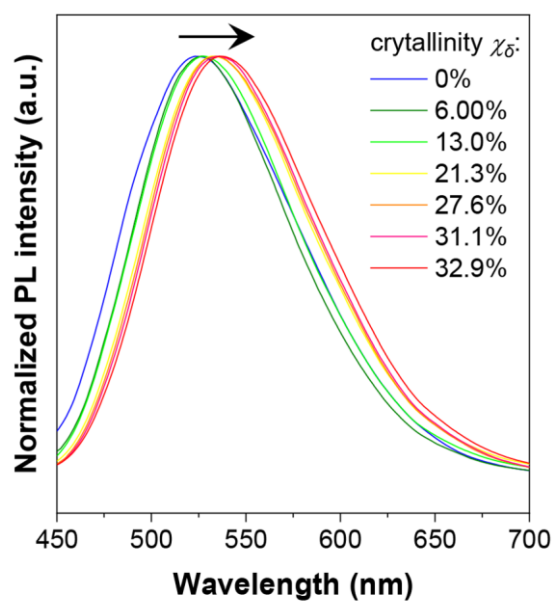


Figure S8. Normalized PL spectra of TPE-EP-doped PLLA δ crystal form at different crystallinities. $\lambda_{em} = 400$ nm.

Table S3. Thermal parameters of TPE-EP-doped PLLA α crystal form with increasing crystallization time.

Crystallization time (min)	T_c (°C)	ΔH_c (J g ⁻¹)	T_m (°C)	ΔH_m (J g ⁻¹)	χ_α (%)
0	112.9	-38.0	171.2	38.0	0
7	112.1	-35.0	171.0	39.9	4.60
10	114.2	-30.8	170.7	45.0	13.4
20	111.7	-16.2	169.6	44.1	26.3
30	113.8	-7.3	169.9	46.5	37.0
60	/	/	169.6	51.1	48.2
90	/	/	170.6	59.6	56.2

Table S4. Thermal parameters of TPE-EP-doped PLLA δ crystal form with increasing crystallization time.

Crystallization time (min)	T_c (°C)	ΔH_c (J g ⁻¹)	$T_{\delta \rightarrow \alpha}$ (°C)	$\Delta H_{m, \delta \rightarrow \alpha}$ (J g ⁻¹)	T_m (°C)	ΔH_m (J g ⁻¹)	χ_δ (%)
0	112.9	-38.0	/	/	171.2	38.0	0
2	106.8	-17.9	154.8	-1.0	169.0	25.9	6.60
4	103.5	-9.0	155.2	-1.8	169.0	26.2	14.5
15	100.2	-1.1	151.5	-3.2	169.1	32.9	27.0
30	/	/	150.8	-3.3	168.5	33.4	28.4
45	/	/	150.9	-3.4	168.5	35.1	29.9
60	/	/	150.6	-3.8	168.7	37.5	31.8

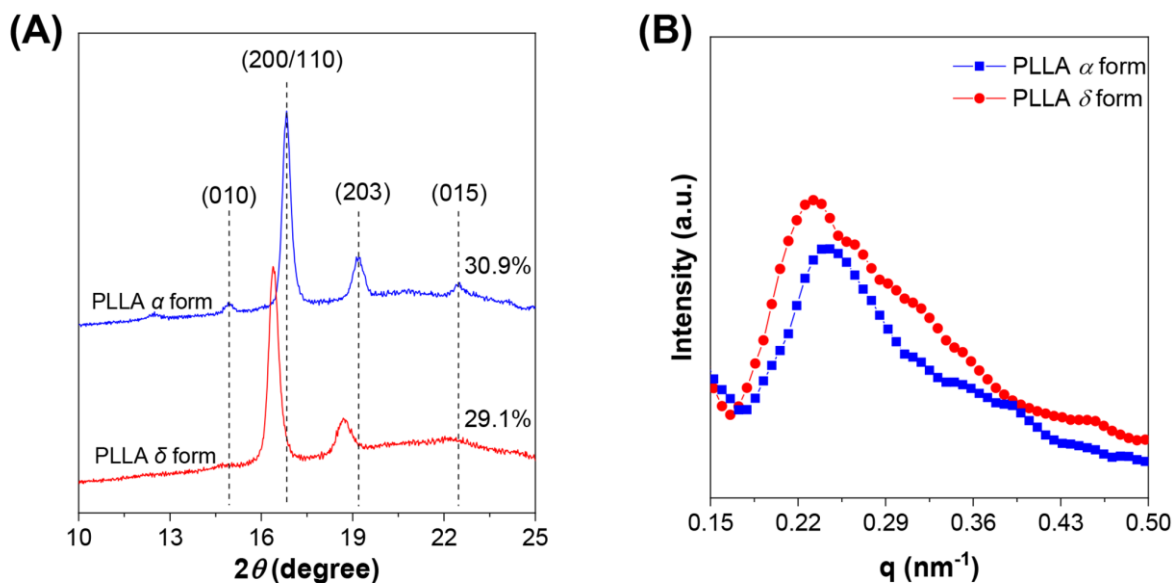


Figure S9. (A) WAXD and (B) SAXS patterns of PLLA α and δ crystal forms at the same crystallinity ($\sim 30\%$).

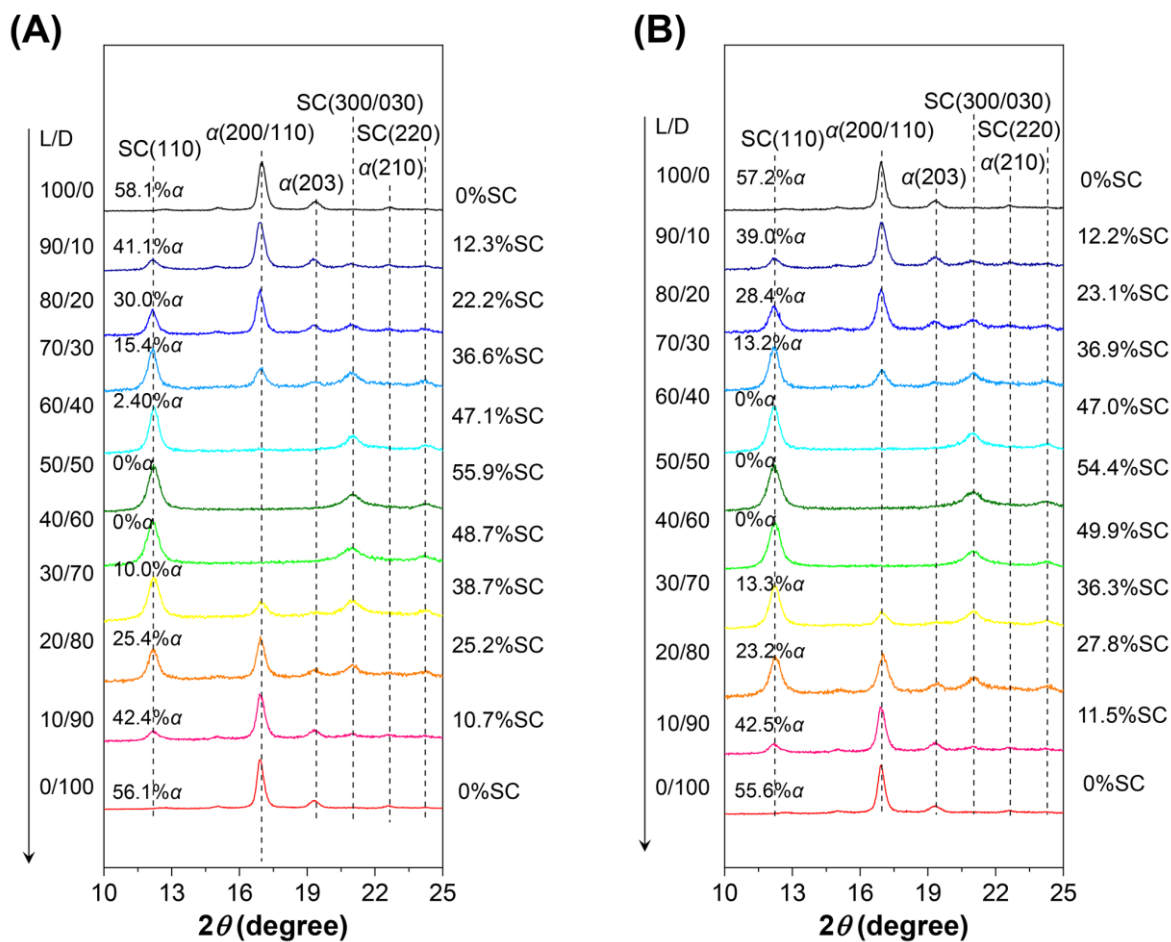


Figure S10. WAXD profiles of PLLA/PDLA blends in parallel experiments.

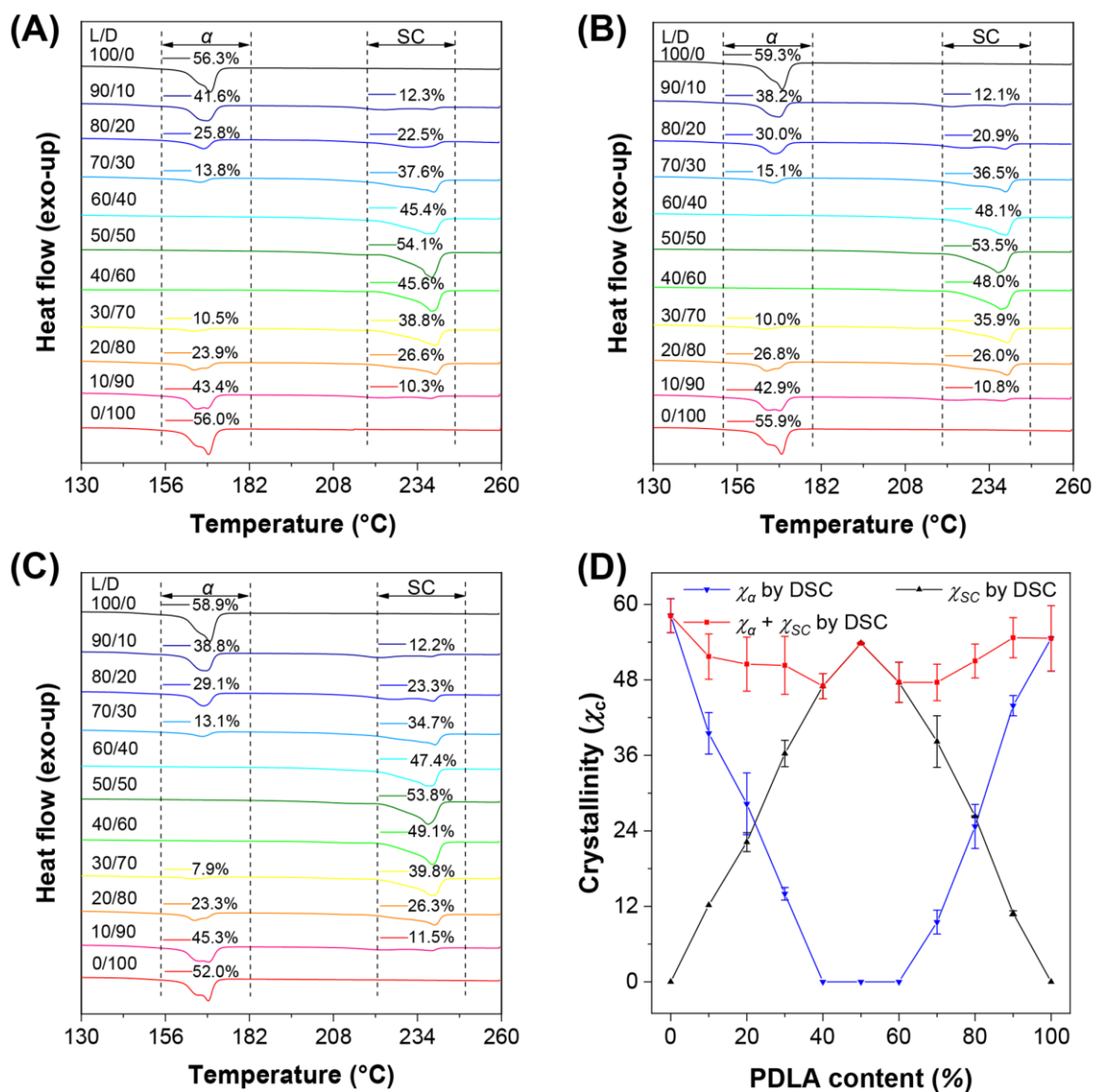


Figure S11. (A-C) DSC thermograms (first heating scan) measured for PLLA/PDLA blends with various L/D ratios in three parallel experiments. (D) Change of the crystallinity of χ_α , χ_{SC} , and $\chi_\alpha + \chi_{SC}$ of PLLA/PDLA blends with various L/D ratios.

Table S5. Thermal parameters of the PLLA/PDLA that correspond to the DSC data in Figure S11A.

L/D	$T_{m,a}$ (°C)	$\Delta H_{m,a}$ (J g ⁻¹)	χ_a (%)	$T_{m,SC}$ (°C)	$\Delta H_{m,SC}$ (J g ⁻¹)	χ_{SC} (%)	χ_{a+SC} (%)
100/0	169.8	59.7	56.3	/	/	0	56.3
90/10	168.9	44.1	41.6	224.1; 238.5	17.4	12.3	53.9
80/20	167.9	27.4	25.8	223.2	32.0	22.5	48.3
70/30	166.7	14.6	13.8	239.0	53.4	37.6	51.4
60/40	/	/	0	237.1	64.5	45.4	45.4
50/50	/	/	0	238.4	76.8	54.1	54.1
40/60	/	/	0	238.4	64.7	45.6	45.6
30/70	164.6	11.1	10.5	239.6	55.1	38.8	49.3
20/80	165.0	25.3	23.9	239.6	37.8	26.6	50.5
10/90	165.8	46.0	43.4	223.9; 238.3	14.6	10.3	53.7
0/100	169.3	59.4	56.0	/	/	0	56.0

Table S6. Thermal parameters of the PLLA/PDLA that correspond to the DSC data in Figure S11B.

L/D	$T_{m,a}$ (°C)	$\Delta H_{m,a}$ (J g ⁻¹)	χ_a (%)	$T_{m,SC}$ (°C)	$\Delta H_{m,SC}$ (J g ⁻¹)	χ_{SC} (%)	χ_{a+SC} (%)
100/0	169.9	62.9	59.3	/	/	0	59.3
90/10	168.8	40.5	38.2	222.6; 238.3	17.2	12.1	50.3
80/20	167.7	31.8	30.0	227.8; 238.8	29.7	20.9	50.9
70/30	167.0	16.0	15.1	239.0	51.9	36.5	51.6
60/40	/	/	0	239.0	68.3	48.1	48.1
50/50	/	/	0	236.7	75.9	53.5	53.5
40/60	/	/	0	237.6	68.2	48.0	48.0
30/70	164.5	10.6	10.0	239.6	51.0	35.9	45.9
20/80	165.2	28.4	26.8	239.5	36.9	26.0	52.8
10/90	169.2	45.5	42.9	224.2; 238.6	15.4	10.8	53.7
0/100	169.7	59.3	55.9	/	/	0	55.9

Table S7. Thermal parameters of the PLLA/PDLA that correspond to the DSC data in Figure S11C.

L/D	$T_{m,a}$ (°C)	$\Delta H_{m,a}$ (J g ⁻¹)	χ_a (%)	$T_{m,SC}$ (°C)	$\Delta H_{m,SC}$ (J g ⁻¹)	χ_{SC} (%)	χ_{a+SC} (%)
100/0	169.7	62.4	58.9	/	/	0	58.9
90/10	168.6	41.1	38.8	223.1; 238.3	17.3	12.2	51.0
80/20	167.8	30.8	29.1	227.5; 238.8	33.1	23.3	52.4
70/30	167.4	13.9	13.1	239.4	49.3	34.7	47.8
60/40	/	/	0	237.4	67.3	47.4	47.4
50/50	/	/	0	237.3	76.4	53.8	53.8
40/60	/	/	0	238.6	69.7	49.1	49.1
30/70	164.6	8.4	7.9	239.0	56.5	39.8	47.7
20/80	165.1	24.7	23.3	239.4	37.4	26.3	49.6
10/90	169.4	48.0	45.3	224.6; 238.5	16.4	11.5	56.8
0/100	169.3	55.1	52.0	/	/	0	52.0

Table S8. Fluorescence spectral data of a range of TPE-EP-doped PLLA/PDLA samples.

L/D	Emission maximum (nm)				
	first group	second group	third group	average	variance
100/0	554	555	552	553.7	2.3
90/10	547	546	546	546.3	0.3
80/20	544	544	543	543.7	0.3
70/30	540	540	540	540.0	0
60/40	536	536	536	536.0	0
50/50	558	558	560	558.7	1.3
40/60	538	535	536	536.3	2.3
30/70	538	535	537	536.7	2.3
20/80	542	544	541	542.3	2.3
10/90	550	550	551	550.3	0.3
0/100	552	552	549	551.0	3.0

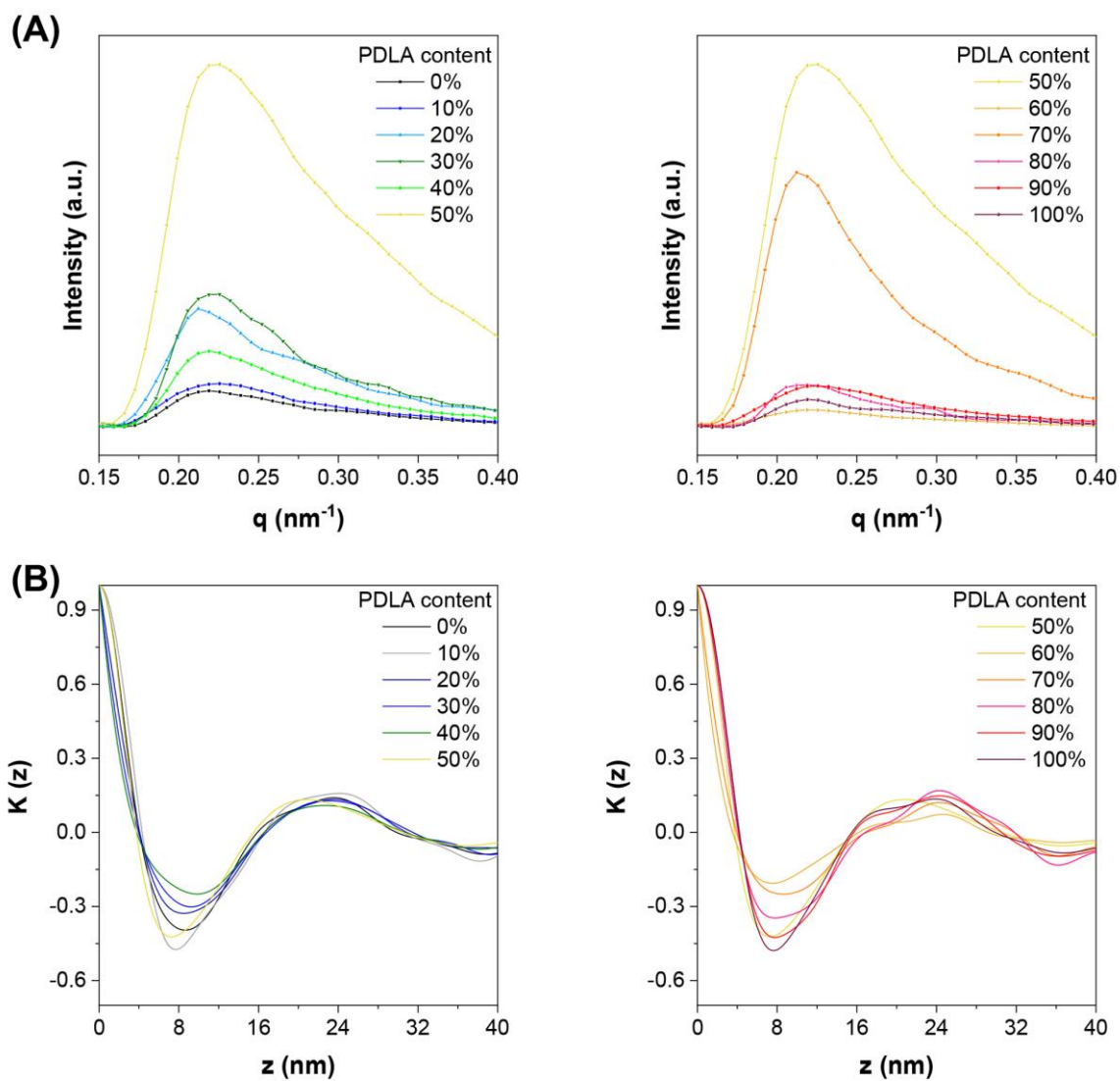


Figure S12. (A) SAXS patterns and (B) corresponding one-dimensional correlation function profiles of the PLLA/PDLA blend samples.

Table S9. The long period (L), the crystal thickness (L_c), and the amorphous layer thickness (L_a) of PLLA/PDLA blend samples.

L/D	L (nm)	L_c (nm)	L_a (nm)
100/0	23.6	5.5	18.1
90/10	24.1	5.9	18.2
80/20	23.6	5.1	18.5
70/30	23.0	3.6	19.3
60/40	22.7	2.9	19.8
50/50	20.8	5.0	15.8
40/60	24.6	2.7	22.0
30/70	24.3	3.7	20.6
20/80	24.3	5.2	19.1
10/90	24.3	5.6	18.8
0/100	23.9	5.8	18.1

Supplementary References

1. J. R. Sarasua, R. E. Prud'homme, M. Wisniewski, A. L. Borgne, N. Spassky, *Macromolecules* **1998**, 31, 3895.
2. H. Tsuji, F. Horii, M. Nakagawa, Y. Ikada, H. Odani, R. Kitamaru, *Macromolecules* **1992**, 25, 4114.
3. H. Tsuji, *Macromol. Biosci.* **2005**, 5, 569.
4. G. R. Strobl, M. Schneide, *J. Polym. Sci., Polym. Phys. Ed.* **1980**, 18, 1343.
5. M. Khorloo, Y. H. Cheng, H. K. Zhang, M. Chen, H. H. Y. Sung, I. D. Williams, J. W. Y. Lam, B. Z. Tang, *Chem. Sci.* **2019**, 11, 997.